International Forum on Aeroelasticity and Structural Dynamics
IFASD 2017
25-28 June 2017 Como, Italy

DESIGN AND TESTING OF A FULL SPAN AEROELASTIC WIND TUNNEL MODEL

Ulf Ringertz[1], David Eller[1], Donald F. Keller[2], Walter A. Silva[2]

[1]Department of Aeronautical and Vehicle Engineering
Kungliga Tekniska Högskolan (KTH), Stockholm, Sweden

[2]Aeroelasticity Branch, NASA Langley Research Center
Hampton, Virginia, USA

Keywords: Transonic, wind tunnel, flutter, aeroelasticity

Abstract: An aeroelastic wind tunnel model has been designed and built for testing in the Transonic Dynamics Tunnel. The aircraft configuration represents a modern light weight fighter with a swept wing and canards. The model is designed using composite materials for all lifting surfaces and the fuselage shell. The lifting surfaces are attached to an internal backbone structure using aluminum spars and bulkheads to transfer the aerodynamic loads to the sting. The wing design is also made with a strong internal frame to provide strong support for external stores without giving too stiff overall wing properties. External stores interfaces in the form of pylons, sway braces and pre-tension arrangements are modeled with additional detail to provide realistic kinematics.

The model is heavily instrumented with accelerometers, strain gauges, and pressure taps. A unique feature of the test set-up was the use of an optical motion tracking system that made it possible to accurately measure model deformations during wind tunnel testing. A new system for unsteady pressure measurements was also used for the test providing accurate unsteady pressure data from almost 200 pressure taps on the wing surfaces. Wind tunnel testing was performed both in air and heavy gas with the model tested in three different configurations. A large amount of unique data was obtained for both static and dynamic aeroelasticty with simultaneous measurements of model deformation and wing surface pressures.

1 INTRODUCTION

The purpose of the test was to obtain experimental data from aeroelastic testing in transonic conditions. The testing was performed in the Transonic Dynamics Tunnel (TDT) [1] at NASA Langley. The model is to be instrumented with accelerometers, strain gauges and pressure transducers and an air data boom with data acquisition performed in the model. An optical position measurement system is also to be used in order to measure model deformations during testing.

The model represents a modern light fighter configuration similar to the Swedish Saab JAS-39 Gripen. The Gripen was tested for flutter clearance in the TDT during the period

1985-1987. For that test, two models were designed and built, a stiff stability model with correct geometry and mass properties, and a flutter model with also correctly scaled stiffness properties. Both models are still available and are in good condition. These models were originally considered for use in the testing currently in preparation but issues with intellectual property rights encouraged a new design. The new model design is compatible with the original model in that lifting surfaces may be attached to the old fuselage and vice versa. Further, the availability of the original model systems report [2] was also useful in the design of the new model.

This paper presents the model design, manufacturing and testing that was performed to satisfy TDT facility requirements [3] and the objectives of the wind tunnel testing. A general overview of the model design is first presented followed by a more detailed description of construction techniques, analysis and testing performed.

2 GEOMETRY

The overall geometry was first designed using the preliminary design tool *sumo* developed by David Eller [4]. This design tool provides surface geometry that is compatible with grid generation tools for Computational Fluid Dynamics (CFD) analysis. The surface geometry provided by *sumo* is then transferred to a commercial CAD system [5] for detailed structural design.

The overall geometry of the model is shown in Figure 1 using the CAD system geometry.

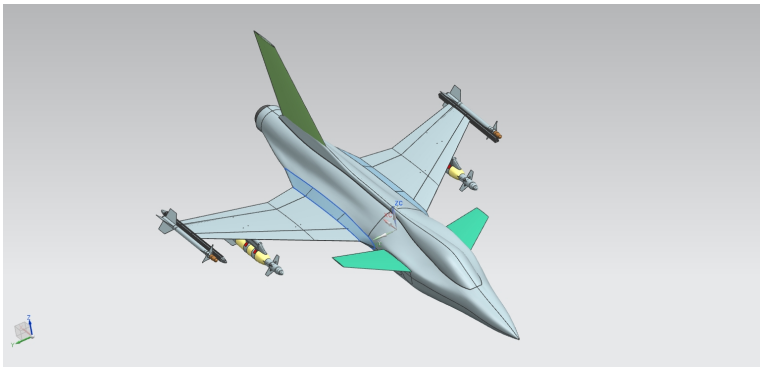

Figure 1: Computer definition of model geometry.

The aerodynamic grids, see Figure 2, are generated using the geometry provided by *sumo* which is better for this purpose since it uses properly connected surfaces without leaks. The CFD analysis is the main source of aerodynamic loads data that is used for both structural analysis and proof-loading.

The structural analysis Finite Element Method (FEM) model is shown to the right in Figure 2. The FEM model is assembled with a mix of solid, shell and beam elements and is generated using a mixture of in-house tools. The FEM model data is prepared using basic Nastran input format so that different versions of Nastran can be used for

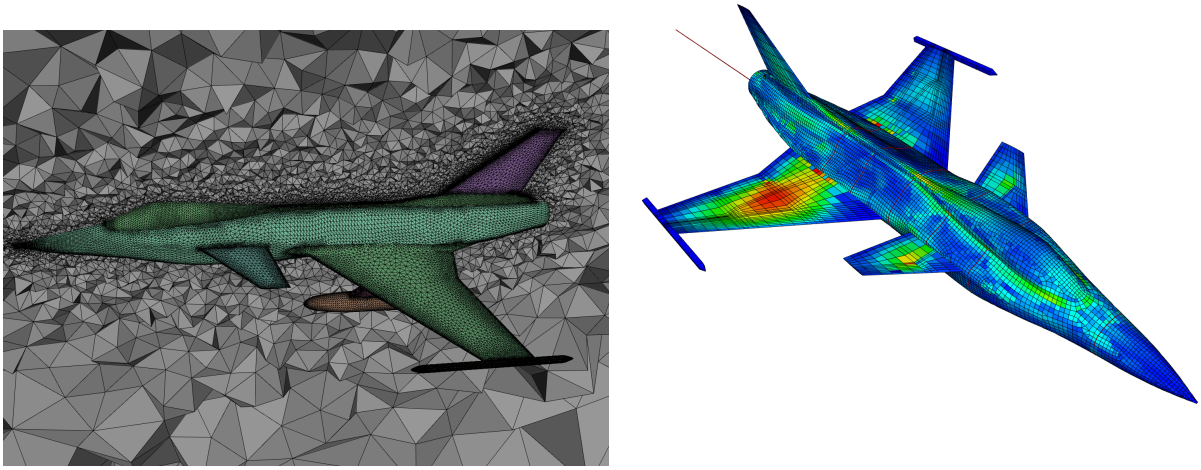

Figure 2: CFD mesh for configuration with drop tanks and Nastran model.

the analysis. The main purpose of the FEM model is accurate stiffness and structural dynamics for the simulation of aeroelasticity. Consequently, the stresses and strains obtained with the model are not considered very accurate.

3 STRUCTURAL CONCEPT

The fuselage of the model is formed by a rather stiff shell of carbon fiber epoxy composite with an internal support using a pair of aluminum spars attached to the steel sting adapter. The sting adapter is then attached to the sting number 7 in the TDT inventory. The sting adapter was designed and used for the original Gripen model tested in the 1980s. The loads from all lifting surfaces are directly transferred to the central spars and the sting as shown in Figure 3.

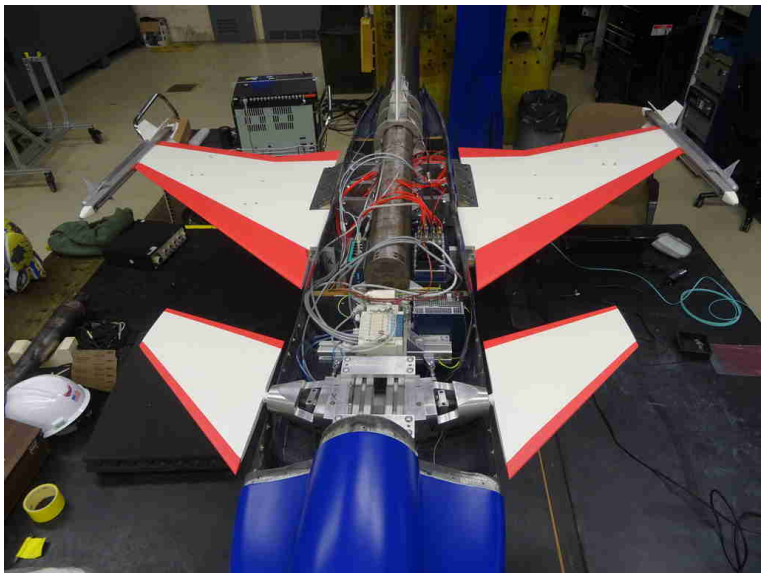

Figure 3: Load path from lifting surfaces to sting.

The fuselage shell is designed with a stiff epoxy carbon fiber composite shell structure with bulkheads that are attached to the main spars and the sting. The fuselage shell is not supporting any loads from the lifting surfaces in order to provide a well defined interface for the load transfer to the sting supporting the entire model assembly. The fuselage shell is split in several parts for easier shipment and also to allow removal of the rear fuselage shell when mounting the sting adapter to the sting in the test section.

3.1 Wing structure

The wing structure is designed as a composite sandwich structure with an internal skeleton to support concentrated loads from external stores. The internal skeleton, see Figure 4, of 4 mm thick fiberglass epoxy laminate is cut to precise shape using a water-jet cutting technique. The skeleton has a few slender beams to maintain shape during cutting and handling. These beams are removed after that the skeleton has been glued to one side of the sandwich foam. This design also provides some openings for running cables inside the wing, also after final assembly of the wing structure. The foam parts

Figure 4: Internal wing skeleton structure.

for the wing are milled from CAD geometry data and are made of H200 high density Divinycell foam [6]. This foam has good properties for a flutter model since it is linear elastic to large strains and also features high failure strain. The moulds used for geometry definition and assembly were also computer cut from CAD geometry data. The foam outer faces are covered with a thin fiberglass epoxy laminate to achieve sufficient strength and appropriate stiffness.

4 TEST CONDITIONS

The model was tested sting mounted in the TDT test section using sting number 7 as shown in Figure 5. The design dynamic pressure is 10 kPa or approximately 208 psf. Testing was performed in the TDT Mach number range of 0-1.2 in various levels of static pressure to give bounded dynamic pressure.

Angle of attack α may be adjusted in the range -5 to 5 degrees when running at the design dynamic pressure. There was no intention of testing with side slip but loads

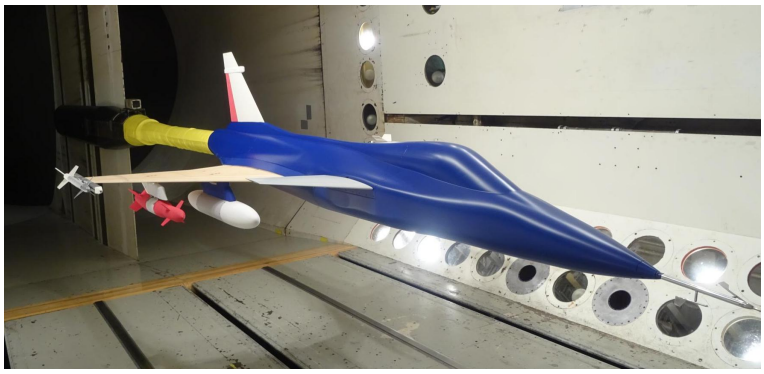

Figure 5: Model on sting.

under side slip conditions were analyzed for additional model safety. Maximum side slip β in the loads analysis was assumed to be 5 degrees.

5 INSTRUMENTATION

Several new measurement and data acquisition systems were used during the testing of the KTH model. The pressure measurement system [7] was new to both NASA and KTH although it is a development of systems currently used at NASA and KTH. The optical deformation measurement system [8] has been used at KTH, but never in the TDT. Another new system in use was the compact RIO (cRIO) systems [9] that were used to process most analog signals. The idea with using the cRIO systems is to process and digitize the analog signals directly in the model and then distribute the data in digital form to the control room of the wind tunnel using standard high-speed fiber optic Ethernet communication. The advantage with this approach is that analog wiring is significantly reduced in length and the time needed to prepare the model in the test section can be reduced. However, it was not known prior to the test how well the cRIO systems and the cameras for the optical system would cope with the rather harsh environment in the TDT with low pressure, heavy gas and vibration. Consequently, for model safety purposes, some extra accelerometers were installed in the model with long wires connected to the tunnel facility data acquisition system AB-DAS [10]. The AB-DAS system records shorter data sets following a trigger command from one of the test engineers. There is also a ring buffer that makes sure that the most recent data is stored if any of the emergency switches is pressed.

The KTH data acquisition systems were set up differently. Data was continuously streamed over the local KTH Ethernet using the UDP broadcast protocol. Whenever the wind tunnel model was powered up, data was streamed from the on-board data acquisition systems and any computer on the local network could read and store the incoming data as desired. In most cases, data was continuously stored on several computers for redundancy. In order to avoid excessively large files, data storing was stopped occasionally, when appropriate, and then restarted to create new data files.

The pressure measurement system and the optical deformation measurement systems were also set up for continuously streaming data over the Ethernet but using special

TCP/IP protocols so that data could only be recorded by one computer at a time. However, the pressure measurement system computer was set up and programmed to redistribute the recorded data so that it could be stored also on an additional computer.

Most of the analog channels were connected to the modular cRIO systems installed in the model fuselage as shown in Figure 6. Approximately 200 pressure taps were

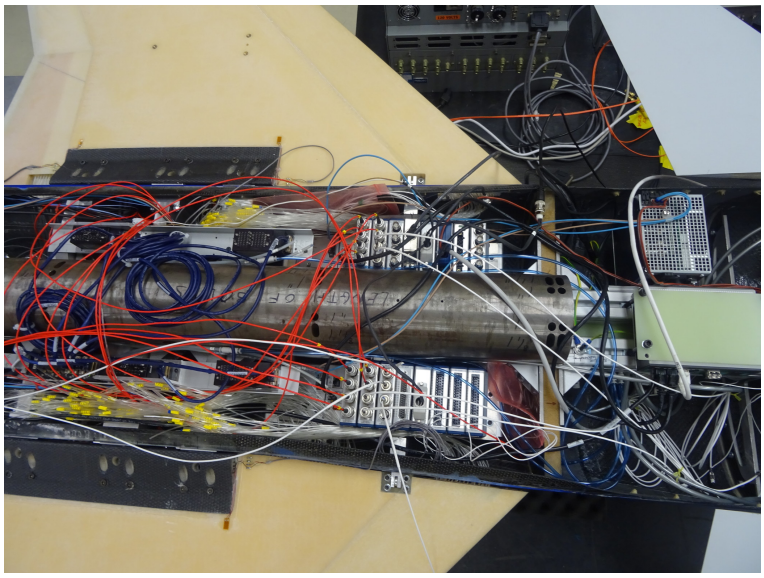

Figure 6: Model internal data systems.

installed in the wings located at two chord stations on each wing. Each pressure tap was connected to the scanner [11] in the fuselage using stainless steel tubing in the wing and plastic tubing from the wing root to the scanner in the fuselage.

A unique feature of the test was the use of an optical motion tracking system [8] to accurately measure model deformations. The system uses a set of motion capture cameras to identify optical markers. The markers may be passive reflective or active in the form of a small light emitting diode (LED). The passive markers often need to be spherical for good accuracy and for the present test these protruding markers would both locally distort the flow and may also not be sufficiently strong structurally to stay in place on the model at higher dynamic pressures. Consequently, active markers were chosen as illustrated in Figure 7.

The drawback with the active marker is that 5 volt power needs to wired to each marker. The markers were typically placed in recessed holes that were designed into the parts that were 3D printed giving accurate positioning of the markers.

The cameras need to be mounted so that all cameras see all markers for best system performance. In the test section of the TDT, there are numerous holes with glass windows used for lights. Four of these lights were removed and the cameras were installed in their place as shown in Figure 7. This position worked well and it was possible to arrange both cameras and markers so that they were all in view.

Also the external stores were instrumented with accelerometers. Tri-axial accelerome-

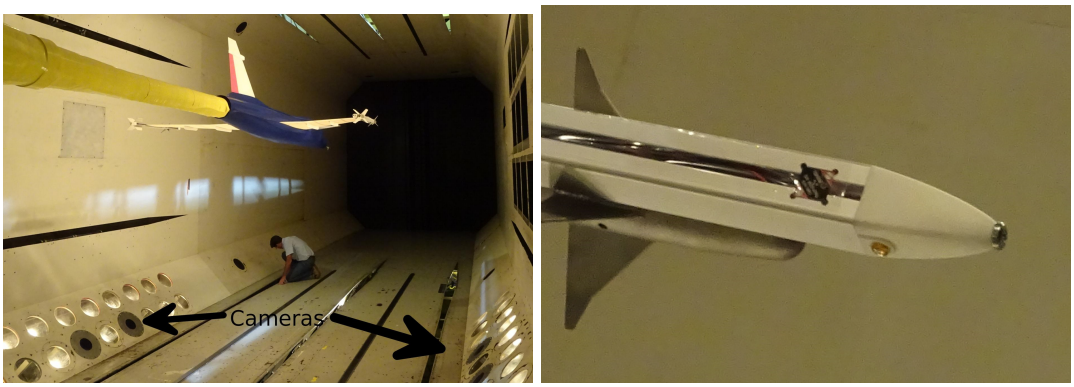

Figure 7: Optical system in the tunnel test section and marker in wing tip pylon.

ters were installed inside the pylon, as shown in Figure 8, and also at each end of each store. The Figure also shows the load cells that were used to measure the pre-tension of the store to the sway braces. The pre-tension can be adjusted and the sway braces are designed in a modular fashion making it possible to obtain different stiffness and friction properties.

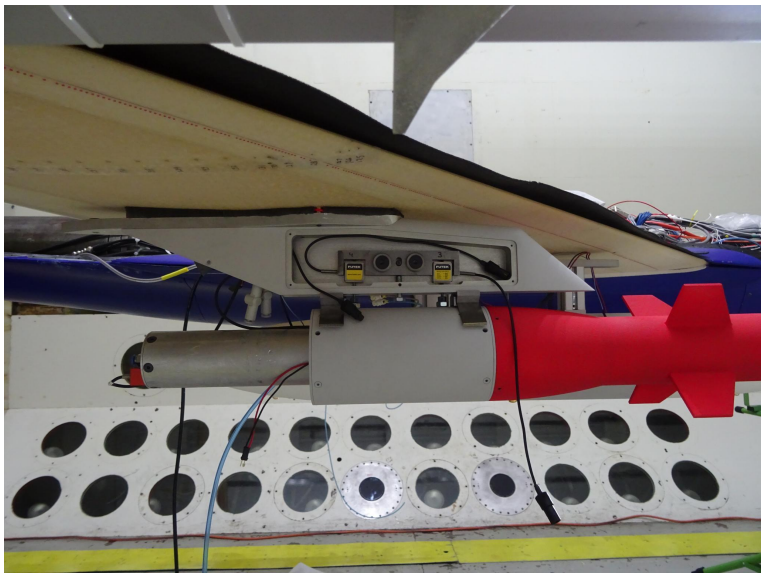

Figure 8: GBU in partial assembly with internal load cells.

6 FINITE ELEMENT MODEL

A NASTRAN finite-element model of approximately 18 000 shell, solid and beam elements was assembled in order to determine load distribution resulting from static aerodynamic loading (see Figure 2). This analysis model is deemed sufficiently well developed with respect to static stiffness, but its mass distribution is not entirely accurate. Due to the rather coarse element size, stresses computed are thus regarded as approximate values.

All lifting surfaces are modeled as solid (foam) and shell (skin) elements. Additional

shell elements are introduced for the internal structure of the wings seen in Figure 4. The fuselage is modeled with simplified internal reinforcements represented by beam elements and without accounting for additional carbon fiber layers present near the joints. It is assumed that the fuselage shell is weaker than the wind tunnel model fuselage, especially near load introduction points and seams. External stores are not explicitly included in the finite-element model, but analyzed separately.

The stiffness of the model was measured using the optical deformation measurement system as shown in Figure 9. Passive reflective markers were placed on the wings and canard surfaces and motion of the markers was tracked as dead weights were applied as loads. Loads were applied in the same position as the markers whenever practical in order to generate a matrix of flexibilities. The FEM model was then loaded in the same manner so that the flexibilities could be compared. Slight tuning of the uncertain foam modulus and composite shell thickness was used to tune the FEM model.

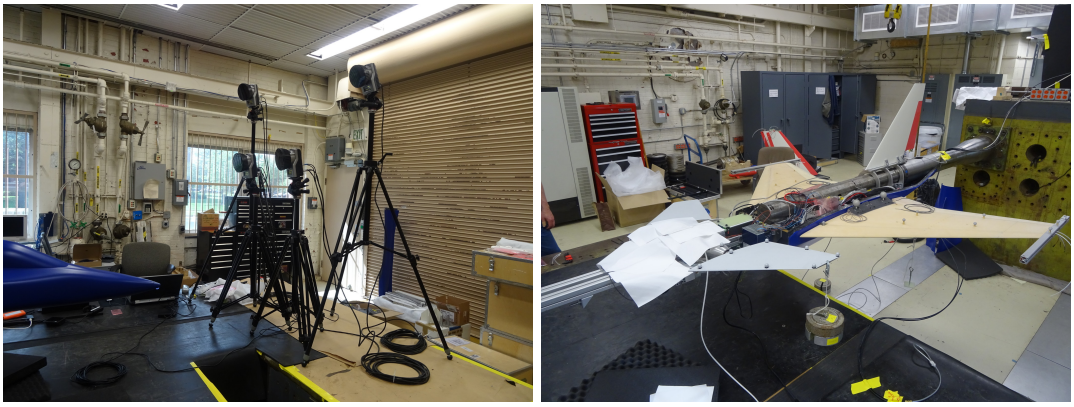

Figure 9: Model stiffness testing using the optical system.

6.1 Sting support

For the static load analyses, the boundary conditions imposed by the flexible sting support in the TDT were found to be of less importance since conservative aerodynamic loads could be determined from a rigid aircraft geometry. For the stability analyses shown in Section 9, however, at least an approximation (linearisation) of the rather complex structural properties of the support needs to be included.

Static deflection tests of the model mounted on sting 7 were performed in the TDT test section using the setup shown in Figure 10. Simultaneously with loading, the motion of the model was tracked by means of the optical measurement system [8]. Figure 11 shows the displacements obtained.

A first-order model for the sting support is defined as a spring with four degrees of freedom (translation and rotation about y and z). Corresponding values of the spring stiffness values were then obtained by matching the observed displacement of the wing-tip markers with the predicted deformation of the finite-element model at the known location of the marker points. Given the considerable non-linearity of the experimental

Figure 10: Sting stiffness testing in the test section.

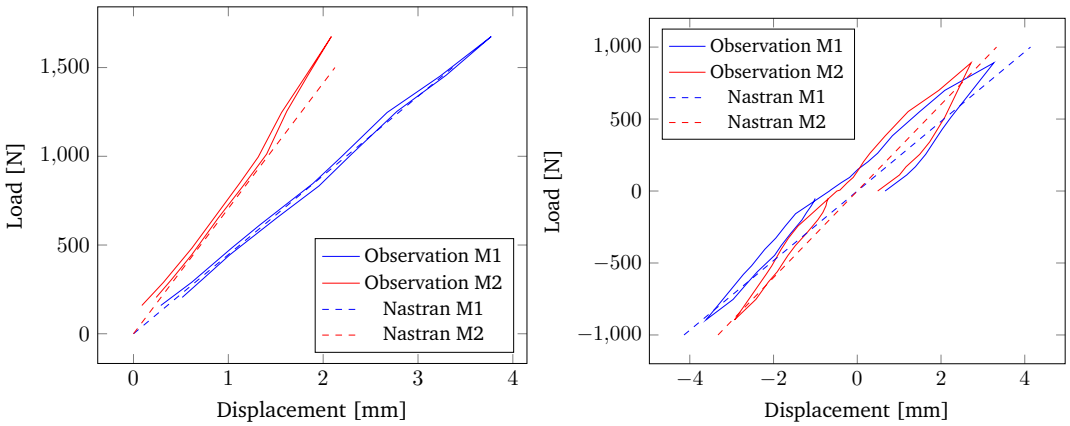

Figure 11: Vertical (left) and lateral (right) displacement of wing-tip markers.

data obtained for lateral loading, such a simple model is certainly a strong simplification, but is considered to be sufficient for linear stability analyses.

Table 1 shows the equivalent static stiffness and equivalent damping values of the grounded spring attached to the downstream end of the sting. Damping constants which approximate the dissipation observed in the case of lateral loading are also given for reference. Further details on the sting modeling is available in a separate report [12].

	DoF	Stiffness k	g [-]
2	Ty	964 kN/m	0.1008
3	Tz	3531 kN/m	-
5	Ry	36.5 MNm/rad	-
6	Rz	2.42 MNm/rad	0.1008

Table 1: Equivalent support stiffness values.

6.2 Dynamic model update

For dynamic stability analyses, the finite element model was updated by adjusting uncertain parameters to better match the results of a ground vibration test (GVT) per-

formed at KTH prior to shipping the model to NASA. Two test setups with 16 accelerometers each were tested. Figure 12 shows the response envelope, that is, the maximum response acceleration value for each frequency, taken over all available accelerometers in each set.

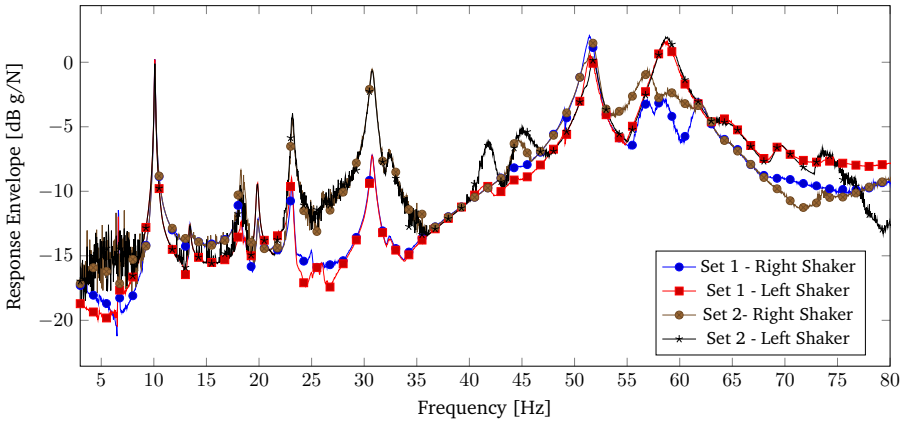

Figure 12: Acceleration response envelope.

For the second set, several wing accelerometers where disconnected and replaced by other accelerometers attached to the vertical fin (measuring lateral acceleration) and the canard surfaces (vertical). The response to excitation is more pronounced in the 20-30 Hz range and shows new peaks at 42 Hz and 45 Hz, which indicates that these responses involve significant motion of canard and vertical fin.

The finite element was updated by modeling the wing tip missiles as beams attached to the tip pylons and attaching concentrated masses matching measured weights of sub-assemblies. Furthermore, the attachment of both canard surfaces and vertical fin were modified to reproduce the observed motion. Table 2 shows the computed eigenfrequencies next to the identified experimental modes. Note that these frequencies are for the spring-suspended model without sting adapter and dorsal fuselage cover. Some

GVT	FEM	Description
10.1 Hz	10.3 Hz	Symmetric wing bending
13.4 Hz	13.9 Hz	Antisymmetric wing bending
-	19.4 Hz	Symmetric bending + canard roll
18.3 Hz	19.8 Hz	Antisymmetric canard roll
19.8 Hz	20.2 Hz	Symmetric wing torsion + canard
23.1 Hz	24.4 Hz	Antisymmetric wing torsion + fin
30.8 Hz	30.0 Hz	Fin + wing torsion
42 Hz	-	Canard motion
45 Hz	-	Canard motion
51.5 Hz	57.8 Hz	Sym. canard + 2nd bending
58 Hz	59.8 Hz	2nd wing bending + canard motion

Table 2: Results for adapted model

of these results are fairly satisfactory. However, the static stiffness of the canard and fin

attachments appear to be not well represented as there still are significant differences especially when motion of the canard surfaces is involved.

7 LOADS ANALYSIS

Loads for the finite-element model described above are obtained by mapping pressure distributions computed by means of Computational Fluid Dynamics (CFD) to the nodes of the structural mesh shown in Figure 2. Pressure distributions are computed by means of the EDGE flow solver [13], which in the present case solved the inviscid Euler equations. For a single condition (Mach 0.9), a comparison with the SU2 solver [14] was performed, which yielded almost identical results.

Pressure loads were computed for a total of 64 different aerodynamic conditions which fill a three-axis grid defined by Mach number M, angle of attack α and side-slip angle β from the sets

$$M = (0.7,\ 0.8,\ 0.85,\ 0.9,\ 0.95,\ 1.0,\ 1.1,\ 1.2), \tag{1}$$

$$\alpha = (-5^\circ,\ 0^\circ,\ 2^\circ,\ 5^\circ) \tag{2}$$

$$\beta = (-5^\circ,\ 0^\circ). \tag{3}$$

In all cases, the canard surface was held in the neutral position. Elastic deformation of the aerodynamic surface was not taken into account at this stage, since this deformation is assumed to reduce loads. Hence, the pressure distributions computed correspond to those of a rigid aircraft model.

A sequence of meshes have been created in order to evaluate the effect of mesh refinement on structural loads. The finest mesh used, with around 1.2 million nodes of which 260'000 on the model surface was deemed acceptable for the purpose of load estimation since the pressure distribution on outboard wing and vertical fin differed little from the next coarser mesh.

For the estimation of aerodynamic loads on the largest external stores, a second mesh was generated which incorporates fuel tanks and pylon geometry. This mesh is shown in Figure 2.

7.1 Whiffletree for wing proof loading

The wing panels represent the most significant structural part with limited structural strength. This is the main difficulty in design of a wind tunnel model for flutter testing since stiffness and strength do not scale favourably to model size. The structural design is also chosen to be simple to manufacture with good quality in terms of properties. To ensure and prove structural strength of the wing panels fairly elaborate structural testing has been performed to demonstrate structural strength. The wings are also designed to be quite flexible with large deformations at high loading but still with sufficient strength. Consequently, deformations may be large making load testing important

to investigate geometrically nonlinear effects not considered in the linear finite element model.

A dedicated test rig was designed and built using the modular aluminum frame structure which is shown in Figure 13. The modular design makes it possible to adjust the

Figure 13: Whiffletree for wing testing.

geometry of the whiffletree making it possible to test load conditions at different Mach numbers. The load distribution appears to be strongly dependent on the Mach number in transonic conditions.

The wing skins are very thin making point load application difficult. Fortunately, the internal support structure for external stores attachments is quite strong making it suitable for supporting the loads from the whiffletree. The finite element model is used to compute the point load magnitudes as follows. The finite element solution is given by

$$Ku = f, \tag{4}$$

where K represents the stiffness matrix, u the displacement vector and f the applied loading. The distributed loading f is obtained by computational fluid dynamics (CFD) solution for 64 different flight conditions as described before and projected on the finite element structural mesh.

Unit point loads p_i are then applied to the external stores attachment points. There are a total of 3 stations for external stores, one at the wing tip and two for under wing stores. Point loads are applied to both the front and the rear wing pylon attachment positions giving a total of 6 point loads. The displacement vectors u_i are then computed by solving the corresponding additional load cases

$$Ku_i = p_i, \tag{5}$$

on the finite element model. The magnitude of the point loads are then found by solving

the linear least squares problem

$$\min_{c_i} \|u - \sum_i c_i u_i\|, \tag{6}$$

giving the scaling factors in Newtons to be applied to the wing hard points. Using this approach, the displacements, strains and stresses in the structural test rig will be similar to the conditions the model will sustain during the wind tunnel test.

Since the whiffletree is statically determinate, it is straight-forward to compute the attachment point location along the aluminum beams of the whiffletree. Lifting eyes are attached to the aluminum beams in order to connect the different parts of the tree. The aluminum beams and the attachment points of the whiffletree were designed for a maximum total force of 500 kg or 5000 Newtons. The total load is applied using a manual lever chain hoist and the load is measured by a load cell.

The wing is strong but quite flexible as shown in Figure 13 where the load is two times the design load. The strain and wing tip deformation is measured up to a maximum load of approximately 500 kg or 5000 Newtons. At maximum load, the maximum compressive strain is approximately 0.8% suggesting that the ultimate load the wing can carry is approximately 20% higher. The results are presented in Figure 14.

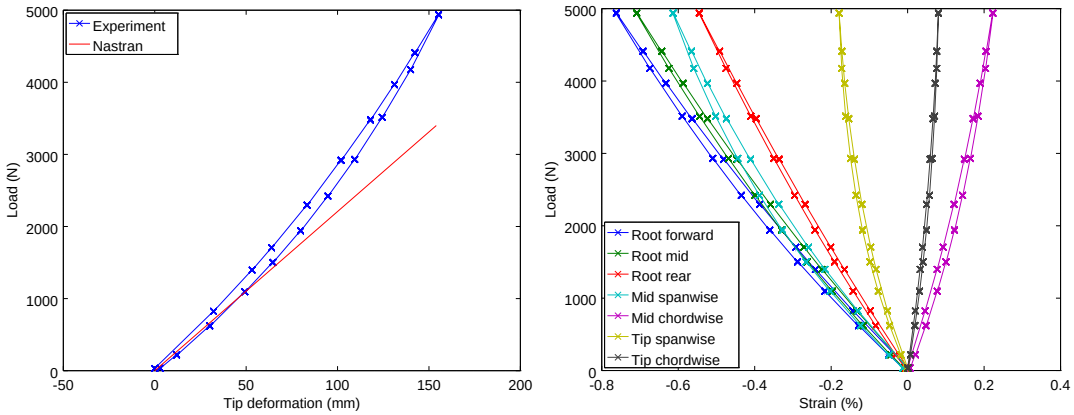

Figure 14: Wing tip deformation and measured strain data.

8 STRESS ANALYSIS

As a design case, the model is assumed to be tested with an angle of attack no more than 5° at a dynamic pressure of 10 kPa (209 psf) or less. Aerodynamic loads for this condition are combined with forces resulting from gravity and then multiplied by a safety factor of 3.0 to obtain an ultimate load case. Stresses found for this ultimate load condition are to be below the ultimate failure stresses of the materials used.

A total of 64 load cases were processed. Different structural components are found to suffer their maximum stress level for different load cases as the pressure distributions changes such that the primary load paths change. However, few components approach stress levels which are relevant from a strength perspective. These selected structural members experience their highest stresses at Mach 0.95, $+5^\circ$ angle of attack and -5° sideslip.

8.1 Aeroelastic considerations

In order to verify the initial assumption that static aeroelastic deformation would lead to a reduction of internal model loads, the computed deformation field was studied. Figure 15 illustrates the deformation expected from a loading corresponding to three times the design load condition. As the plot indicates, it can be expected that the elastic

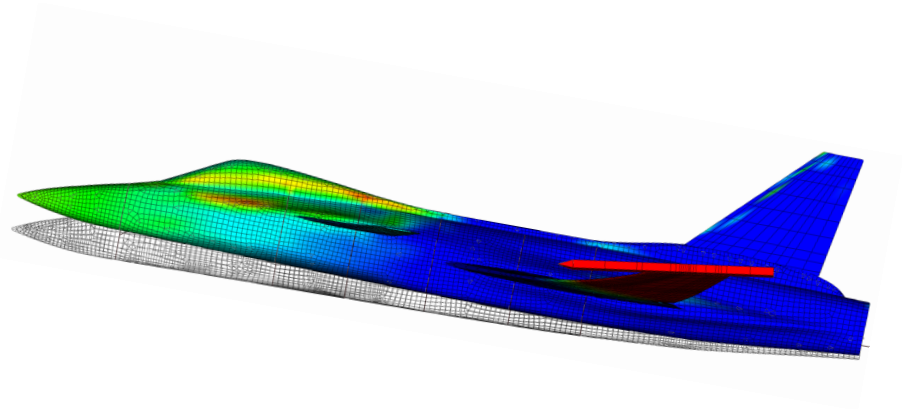

Figure 15: Illustration of model deformation at 3x design load.

nose-down twist of the wings resulting from aerodynamic loads at positive angles of attack will considerably reduce wing loading compared to the simplifying assumption of rigid geometry in the CFD analysis. Due to the flexibility of the model support sting and its attachment to the wind tunnel structure, there is also a counteracting effect which slightly increases the effective local angle of attack over fuselage, canard surfaces and inner wing panel.

With the assumptions made in assembling the finite element model and computing aerodynamic loads, only the main wing shell and the canard (attachment) exhibit stress levels which may reach critical magnitudes.

8.2 Main wing shell

For the critical load condition, compressive stresses in the external upper wing skin reach 132 MPa, which is below the permitted stress of 187 MPa. The highest stress level is reached just outboard of the reinforced patch surrounding the attachment brackets, as illustrated in Figure 16. Due to the sideslip angle applied in this wind tunnel test condition, the loading is asymmetric. Consequently, the windward wing is loaded significantly higher.

9 STABILITY ANALYSES

Aeroelastic stability solutions were performed using NASTRAN. Due to the limitations of the aerodynamic modeling available, the results are not applicable in the transonic regime, where testing will be performed.

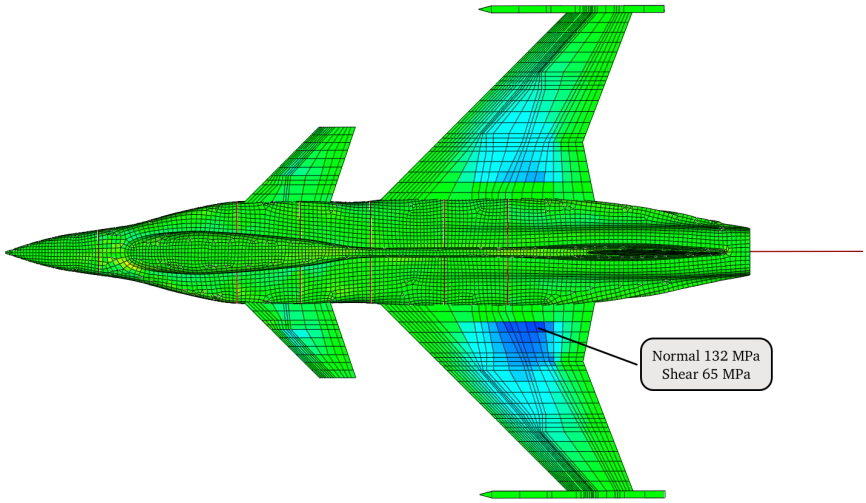

Figure 16: Stress in main wing shell.

9.1 Subsonic divergence

A standard static aeroelastic divergence analysis yields a first critical dynamic pressure at 45 kPa, which is far beyond the TDT envelope. Therefore, it is considered highly unlikely that the model would exhibit divergence at subsonic conditions even at very high dynamic pressure. Due to the significant backward sweep, this result is expected.

9.2 Linear subsonic flutter

There are movable masses in the form of pistons inside the GBU stores and the wing tip missiles. These pistons can be moved between a rear and a forward position using compressed air and valves that are controlled by the model data acquisition system. The lowest critical flutter speed was found with the wing tip pistons in the rear position and the GBU store pistons in the forward position. Figure 17 is a v-g plot for this case computed with NASTRAN and DLM aerodynamics [15] in air at Mach 0.5. The estimated critical flutter dynamic pressure is quite far above the intended maximum dynamic pressure of 10 kPa.

In order to reduce the predicted flutter dynamic pressure, additional mass balancing is required. Fortunately, the model had been prepared for this in that additional ballast masses could be attached to each end of the wing tip pylons. Adding 0.5 kg to each forward end and 0.2 kg to the rear end of the wing tip pylons reduces flutter dynamic pressure significantly, as shown in Figure 18.

Figure 19 shows the expected flutter modes. For many of the cases analyzed there are two modes which become unstable right after another, with the antisymmetric motion from Figure 19 usually becoming unstable at slightly lower dynamic pressure.

10 WIND TUNNEL TESTING

The first days of wind tunnel testing was focused on testing all systems and clearing the model in three different configurations up to design dynamic pressure. Large amounts

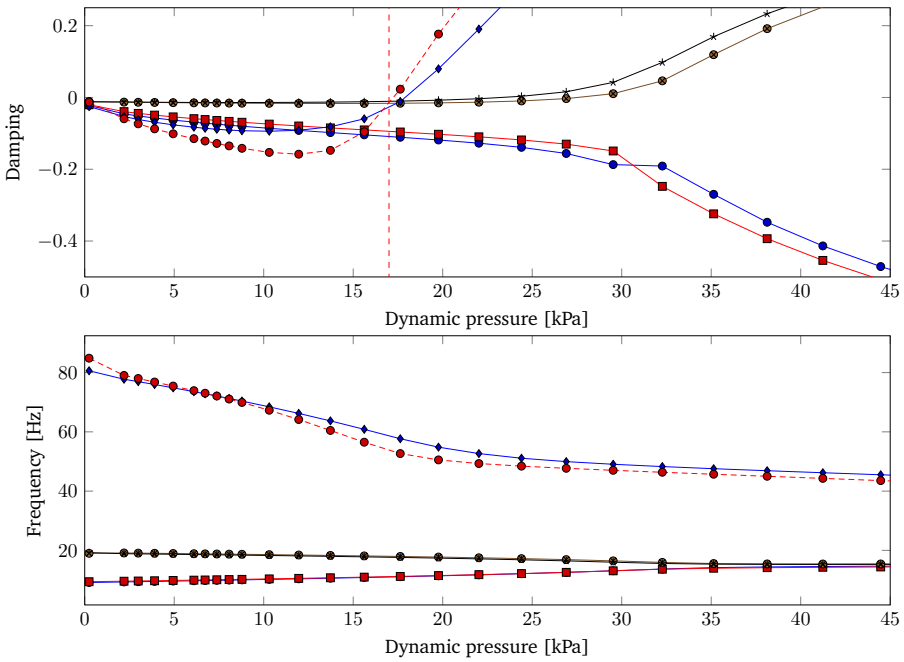

Figure 17: Flutter v-g plot without additional mass balancing.

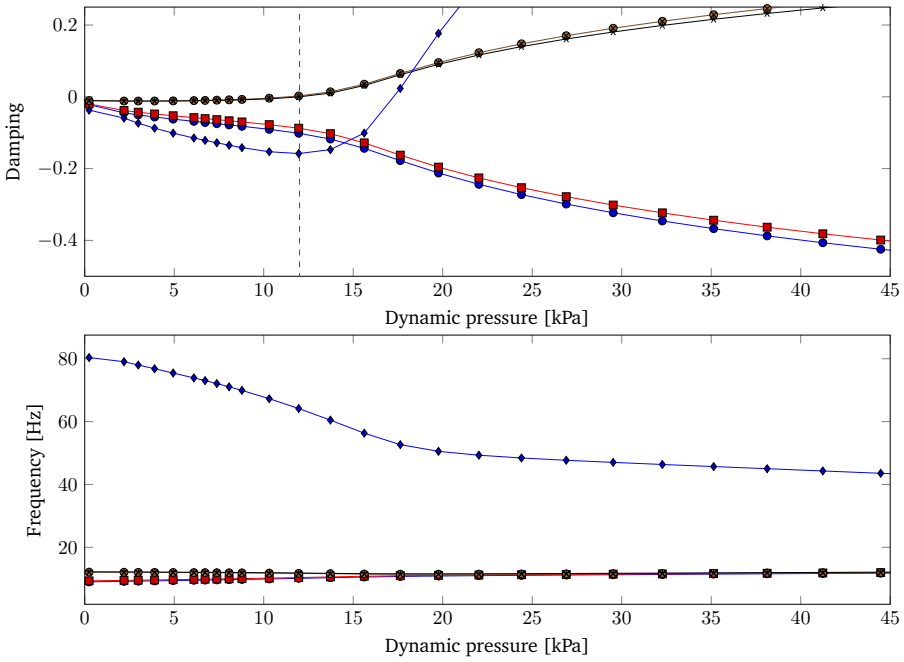

Figure 18: Flutter v-g plot with additional mass balancing.

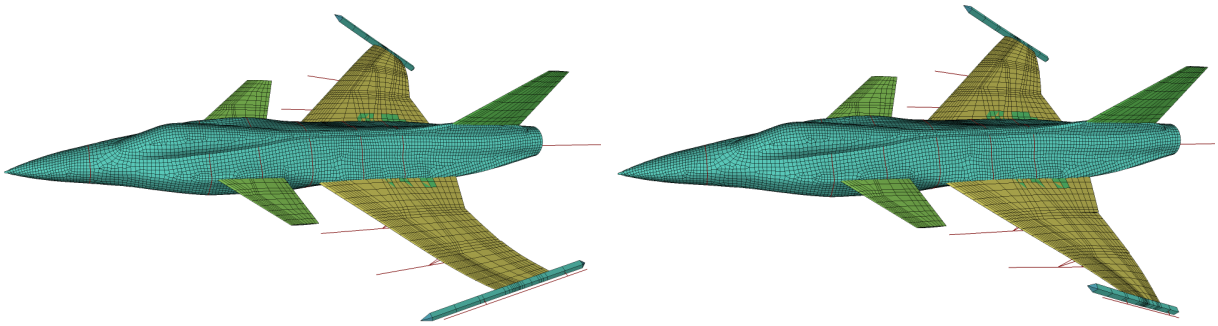

Figure 19: First two flutter modes of the mass-balanced case.

of test data was then acquired for static aeroelasticity with simultaneous measurements of model deformation and pressure data. The model was also excited using the internal shakers in the drop tanks and movement of the canards using pneumatic actuators.

The final day of testing concerned flutter testing. The model was now in the final configuration with all external stores and the mass balancing reducing the predicted flutter dynamic pressure. Two flutter points were recorded in this configuration. In the first flutter case, the divergent motion was stopped in time using the TDT by-pass valves. However, the second flutter point, see Figure 20, was very violent and the by-pass valves were not able to reduce dynamic pressure before the model was damaged.

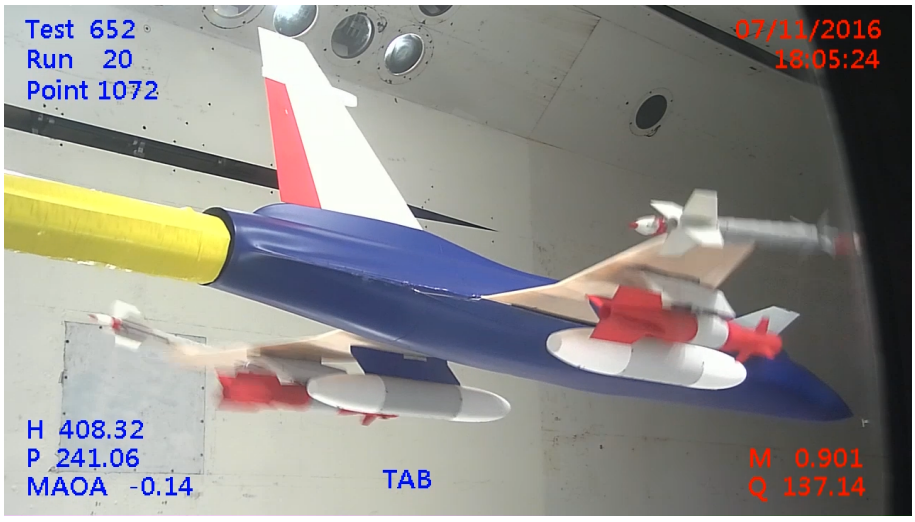

Figure 20: Flutter at Mach 0.9.

Both flutter points were fully recorded by the various data acquisition systems. Figure 21 shows the wing tip markers as recorded by the optical motion capture system and the accelerometer data for the wing tip with maximum acceleration exceeding 50 g. Note that the optical system can not record the markers when deformations get very large since the markers move out of view for the cameras.

The wing skins were damaged in the final flutter test as shown in Figure 22. The wing

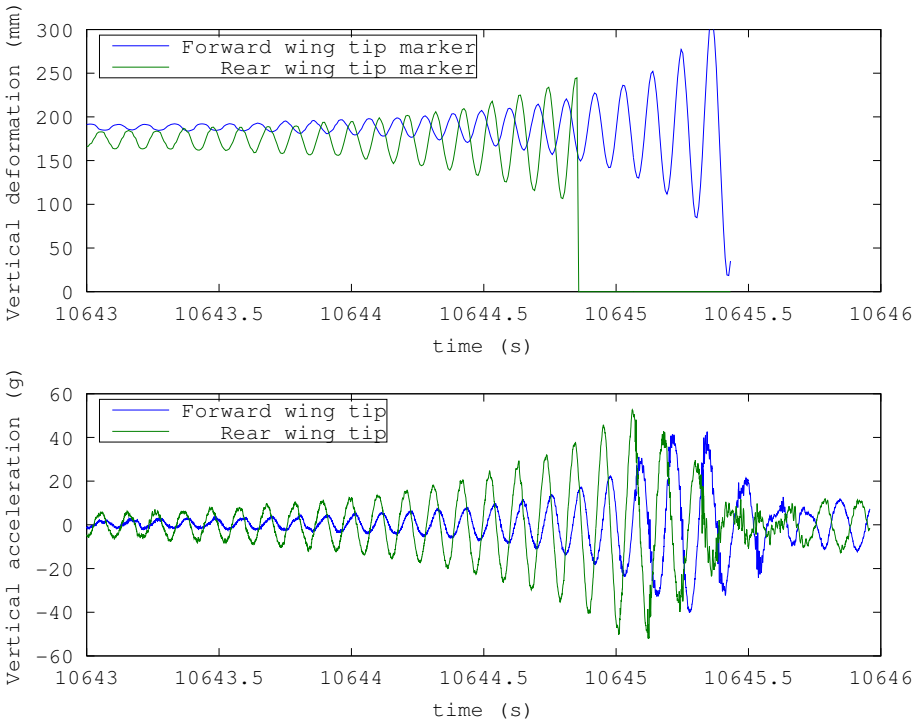

Figure 21: Accelerometer and optical marker data at flutter.

skin laminate is broken but the internal structure is intact and there was no parts of the model breaking off. Consequently, there was no foreign object damage to the wind tunnel.

Figure 22: Wing tip damage.

11 CONCLUSIONS

Performing the test in the TDT was a complex task and the outcome was in many ways better than expected. Prior to the test, the KTH staff had serious doubts about how well the model internal computer systems and the optical camera system would work in the harsh environment with high temperature, sometimes low pressure, heavy gas, and vibrations. However, both these systems worked essentially flawlessly. The internal computer system had one communications failure which turned out to be caused by an optical Ethernet cable that was bent to a sharp kink on its way from the sting to the control room. One of the cameras for the optical system showed some disturbance which was found to be caused by the heat of a light bulb next to it. Once the bulb was removed, there were no further issues.

The structural concept used for the model appears to be a significant success. A flexible, but still very strong wing structure managed to keep all model parts in place, even the heavy external stores, when the model experienced violent flutter with wing tip accelerations exceeding 50 g.

Possibly the most important improvement would be better time accuracy and time stamping of data. Both the TDT and KTH has the hardware in the form of a GPS system [16] that can deliver accurate timing information down to microsecond precision with respect to a global time reference. With all systems referring their data to a common time reference, it is straight-forward to after testing synchronize all data without having to connect the quite different measurement systems and their computers.

ACKNOWLEDGEMENTS

The two first authors from KTH were financially supported by several grants from the Swedish Defense Materiel Administration (FMV) monitored by Curt Eidefeldt and Erik Prisell. Special thanks also to all the staff of the Transonic Dynamics Tunnel for all the support making this effort possible.

12 REFERENCES

[1] NASA Langley Research Center, www.aeronautics.nasa.gov/atp (2009). *Transonic Dynamics Tunnel*. Fact sheet.

[2] Palys, S. (1985). Structural integrity report full span flutter and stability models. Tech. Rep. D-166, Dynamic Engineering Inc., Newport News, VA, USA.

[3] NASA Langley Research Center, Langley Management System (LMS) (2015). *Wind-tunnel model systems criteria*, LPR 1710.15J ed. Expires April 30, 2020.

[4] Tomac, M. and Eller, D. (2011). From geometry to CFD grids—An automated approach for conceptual design. *Progress in Aerospace Sciences*.

[5] (2016). NX for design. http://www.plm.automation.siemens.com.

[6] Group, D. *Divinycell H The high performance sandwich core*. Data sheet, Doc No H June 2015 rev15 SI, www.diabgroup.com.

[7] (2014). *Optimus Pressure Scanning System*. Data sheet, www.meas-spec.com or www.te.com.

[8] Qualisys AB. *Oqus - Qualisys motion capture camera with high-speed video*. Product Information 100, 300 and 500 series, 2011.

[9] National Instruments (2016). *NI cRIO-9068 User manual*. Document 376007B-03, www.ni.com.

[10] Ivanco, T., Sekula, M., Piatak, D., et al. (2016). A new high channel-count, high scan-rate, data acquisition system for the NASA Langley Transonic Dynamics Tunnel. In *54th AIAA Aerospace Sciences Meeting*, no. AIAA 2016-1149 in AIAA SciTech Forum and Exposition.

[11] Pressure Systems, Inc. *ESP Pressure Scanner Users's Manual*. August 2009.

[12] Eller, D. (2016). TDT Sting support: Estimation of stiffness and damping properties. Tech. rep., Department of Aeronautical and Vehicle Engineering. Available on the KTH box.

[13] Eliasson, P. (2002). EDGE, a Navier-Stokes solver for unstructured grids. *Proc. to Finite Volumes for Complex Applications III, ISBN*, 1(9039), 9634.

[14] Palacios, F., Colonno, M., Aranake, A., et al. (2013). Stanford University Unstructured (SU2): An open-source integrated computational environment for multi-physics simulation and design. In *51st AIAA Aerospace Sciences Meeting including the New Horizons Forum and Aerospace Exposition*. Grapevine, TX. AIAA Paper 2013-0287.

[15] Rodden, W. P. and Johnson, E. H. (1994). *Msc.Nastran Aeroelastic Analysis User's Guide.* Los Angeles: MacNeal-Schwendler Corp.

[16] (2016). XL-GPS Time and frequency receiver. www.microsemi.com.

COPYRIGHT STATEMENT